Continuous-wave operation of terahertz quantum-cascade lasers above liquid-nitrogen temperature

Sushil Kumar, Benjamin S. Williams, Stephen Kohen, and Qing Hu[a]
Department of Electrical Engineering and Computer Science and Research Laboratory of Electronics, Massachusetts Institute of Technology, Cambridge, Massachusetts 02139

John L. Reno
Sandia National Laboratories, Department 1123, MS 0601, Albuquerque, New Mexico 87185-0601

We report cw operation of a quantum-cascade laser at 3.2 THz ($\lambda \approx 94$ μm) up to a heat-sink temperature of 93 K. Resonant longitudinal-optical phonon scattering is used to depopulate the lower radiative state and a low-loss metal–metal waveguide is used to provide high modal confinement. Optical powers of $\sim$1.8 mW at 10 K and $\sim$400 μW at 78 K are observed from a single facet of a 40-μm-wide and 1.35-mm-long laser device. A threshold current density of 432 A/cm^2 at 10 K and 552 A/cm^2 at 78 K was obtained in cw mode. The same device lased up to 129 K in pulsed mode with a threshold current density of 419 A/cm^2 at 5 K. © *2004 American Institute of Physics.* [DOI: 10.1063/1.1695099]

Terahertz (1–10 THz, 30–300 μm) frequencies are among the least developed electromagnetic spectra even though they have wide ranging applications in spectroscopy, imaging, and remote sensing. This underdevelopment is primarily due to lack of convenient THz sources that can provide high radiation intensities with cw operation. The recently developed terahertz quantum cascade lasers (QCLs)[1–3] promise to meet this demand. Perhaps the most immediate application for THz QCLs is local oscillators in heterodyne receiver systems, which are widely used in radio astronomy. For such applications, cw operation is required for frequency stabilization and phase locking, and operation above liquid-nitrogen temperature is highly desired. However, there are many challenges to be met to improve the high-temperature performance of THz QCLs. At present, THz QCLs have demonstrated a maximum cw operating temperature of 68 K[4] in a bound-to-continuum[5] type design. For chirped superlattice designs, a maximum cw operating temperature of 48 K has been reported.[6] In this letter, we report cw operation of a THz QCL based on a resonant-phonon design[3] above the liquid nitrogen temperature.

For a THz QCL, the photon energy $\hbar\omega$ for the radiative transition is smaller than the longitudinal-optical (LO) phonon energy ($E_{LO} = 36$ meV in GaAs). Hence, thermally activated LO-phonon scattering leads to a rapid decrease of the upper state lifetime with temperature, which reduces gain in the laser. While the chirped superlattice and bound-to-continuum designs rely on intra-miniband scattering and transport for depopulation of the lower radiative state, this present design uses resonant tunneling and subpicosecond LO-phonon scattering assisted depopulation. Thermal backfilling of the lower radiative state at high temperatures is suppressed in a resonant-phonon design because of the large energy separation ($\geq E_{LO}$) between the lower radiative state and the collector/injector states. Despite a $T_{max} = 87$ K for pulsed operation, the first resonant-phonon design failed to obtain cw operation because of its high threshold current density and voltage ($J_{th} = 806$ A/cm^2, $V_{th} \sim 12.5$ V).[7] The large threshold current density was mostly due to the presence of a parasitic current channel.[8] More recently, pulsed operation up to 137 K was obtained for a resonant-phonon design fabricated using a low-loss, high modal confinement metal–metal waveguide.[9] However, that device suffered from a large thermal resistance at the metallic bonding interface and the formation of high-field domains in the active region, hence cw operation was not achieved.

In the present design, cw operation was obtained up to a heat-sink temperature of 93 K. This was achieved by modifying both the active region and metal–metal waveguide fabrication. Figure 1(a) shows the conduction band diagram for two modules of the device at the design bias. Compared to the similar design in Ref. 3, the 24 Å intra-injector barrier was thickened to 30 Å and the 38 Å collector barrier was thickened to 41 Å. Thickening the intra-injector barrier reduces the coupling between the injector state $n = 1'$ and the excited state $n = 3$ in the wide well of the next module, which reduces the aforementioned parasitic current channel.[8] This also improves the selectivity of injection into the upper radiative state $n = 5$. Thickening the collector barrier, in addition to reducing the parasitic current channel further, also increases the upper state lifetime τ_5 while not affecting τ_4 and τ_3 (as long as the wavefunctions extend coherently across the 41 Å collector barrier). Modifications were also made to the two wide wells in the injector region (occupied primarily by levels 1 and 2) so that the injector doublet is less diagonal at the design bias; as a result it aligns with $n = 5$ at a higher bias as compared to the designs in Refs. 3 and 9. This alignment reduces leakage current at low biases and enhances current transport at higher biases, which prevents the formation of high-field domains that result from negative differential resistance.

The present structure, labeled FL177C-M5, was grown by molecular beam epitaxy (MBE) on a semi-insulating GaAs substrate with 177 cascaded modules to form a 10-μm-thick active region. A 60-nm-thick GaAs contact layer ($n = 5 \times 10^{18}$ cm^{-3}) with a thin low-temperature-grown

---

[a]Electronic mail: qhu@mit.edu

Appl. Phys. Lett., Vol. 84, No. 14, 5 April 2004
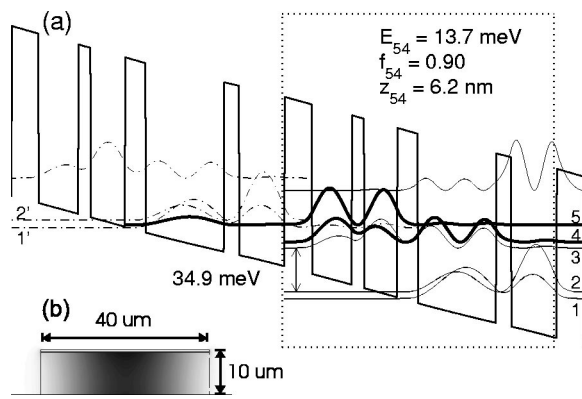
Kumar *et al.* 2495

FIG. 1. (a) Conduction band schematic calculated using a self-consistent Schrödinger and Poisson solver (72% band offset). The four-well module grown in GaAs/Al$_{0.15}$Ga$_{0.85}$As is outlined by the dotted box. Beginning with the left injection barrier, the layer thicknesses in Å are 55/79/25/65/41/155/30/90. The 155 Å well is doped at $n=1.9\times10^{16}$ cm^{-3}, which yields a sheet density of $n=3.0\times10^{10}$ cm^{-2} per module. (b) Grayscale mode intensity for the metal–metal waveguide obtained using a two-dimensional simulation.

GaAs cap layer was grown above the active region in order to allow for the use of a nonalloyed ohmic contact, and a 0.8-μm-thick GaAs contact layer ($n=3\times10^{18}$ cm^{-3}) was grown below. Beneath that, a 0.1-μm-thick undoped Al$_{0.55}$Ga$_{0.45}$As etch-stop layer was grown. This device was then fabricated into a metal–metal waveguide using low temperature In–Au metallic wafer bonding followed by substrate removal, which is described in detail in Ref. 10. The MBE-grown wafer was coated with Ti/Au (20/800 nm) layers and a metal sequence Pd/Ge/Pd/In (25/10/25/1200 nm) was deposited on an n^+ GaAs receptor substrate. Wafer pieces were then cleaved and bonded on a hot plate at 250 °C for 10 min while pressure was applied. Bonding takes place above the In melting point (156.6 °C) as the indium wets the surface, and then diffuses into the gold layer to reactively form a variety of In-Au alloys. In comparison to Refs. 9 and 10 the thin gold layer on top of indium was omitted. Although this gold layer was intended to minimize indium oxidation, it was found to reactively consume much of the indium prior to bonding. The resulting In–Au alloys had high melting points (≥ 450 °C) and they prevented the remaining indium from wetting the interface uniformly during the wafer bonding, which led to the incorporation of voids at the wafer–wafer interface and introduced a large thermal resistance. Following substrate removal of the MBE-grown wafer, upper Ti/Au (20/400 nm) contacts were evaporated on the remaining 10-μm-thick epitaxial layers and dry etching was used to define ridges with nearly vertical side walls. The laser ridge facets were left uncoated. As the last step, the n^+ GaAs substrate was lapped down to a thickness of $\sim$140 μm to improve heat sinking. The calculated mode intensity for a 40-μm-wide waveguide is shown in Fig. 1(b). At 3.2 THz, a waveguide loss of $\alpha_w=17.7$ cm^{-1} ($\alpha_w=18.8$ cm^{-1}) and a confinement factor of $\Gamma=0.92$ ($\Gamma=0.99$) are calculated using a two-dimensional (one-dimensional) solver. Drude-model relaxation times of 0.1, 0.5, and 0.05 ps were used for the heavily doped semiconductor, lightly doped semiconductor, and gold, respectively.

The fabricated devices were indium soldered ridge side up on a copper mount, wire bonded, and mounted on the cold stage in a vacuum cryostat. Figure 2 shows the cw measure-
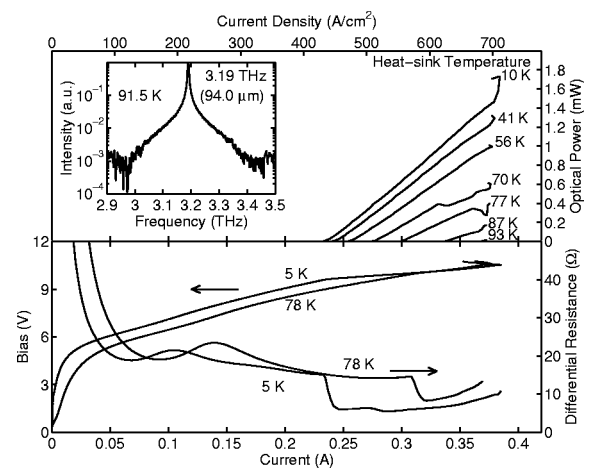

FIG. 2. Continuous-wave characteristics measured from a 40-μm-wide, 1.35-mm-long ridge laser. The upper panel shows the $L-I$ characteristics for various heat-sink temperatures. The inset shows the cw spectrum at a heat-sink temperature of 91.5 K. A Nicolet 850 Fourier transform spectrometer was used with a room-temperature DTGS detector. The linewidth is limited by the spectrometer resolution of 0.125 cm^{-1}. The lower panel shows the cw $V-I$ and $dV/dI-I$ characteristics at heat-sink temperatures of 5 and 78 K.

ment results from a 40-μm-wide, 1.35-mm-long Fabry–Pérot ridge structure that lased up to a heat-sink temperature of 93 K. The fact that this device is the narrowest THz laser to date is testimony to the usefulness of metal–metal waveguide for efficient mode confinement, especially at longer wavelengths. The inset shows a single-mode cw spectrum taken with a room-temperature deuterated triglycine sulfate (DTGS) pyroelectric detector and at a heat-sink temperature of 91.5 K. The laser emission at 3.2 THz corresponds to a transition energy of $\sim$13.0 meV that is slightly smaller than the calculated value of 13.7 meV. The measured light versus current ($L-I$) characteristics are shown in the upper panel of the figure. The threshold current density was $J_{th}=432$ A/cm^2 with a maximum power of $\sim$1.8 mW at 10 K. At 78 K, the threshold current density increased to a value of $J_{th}=552$ A/cm^2 and the maximum output power dropped to $\sim$400 μW. The cw output power from a single facet was collected with a Winston cone and measured with a thermopile detector (ScienTech, Model AC2500) placed directly in front of the cryostat window. The lower panel in Fig. 2 shows the cw voltage versus current ($V-I$) and differential resistance versus current ($dV/dI-I$) plots for the device at 5 and 78 K. The kink in the $V-I$ at threshold is due to a large drop in the differential resistance at onset of lasing. This discontinuity in dV/dI reflects the large difference in upper and lower radiative state lifetimes (calculated low-temperature LO scattering times: $\tau_{5\rightarrow(2,1)}\approx8.0$ ps, $\tau_4\approx\tau_3\approx0.4$ ps) and hence confirms the good selectivity of the injection and depopulation processes.[11] The low-bias dips in the $dV/dI-I$ curves below threshold are due to the parasitic current channel.[8] The corresponding shoulders in the $V-I$ curves are much less pronounced as compared to our previous designs and there is no sign of high-field domain formation; this improvement is attributed to the modified injector design.

Figure 3 shows pulsed $L-I$ characteristics from the same device. The device lased up to a heat-sink temperature of 129 K when biased with 150 ns pulses repeated at 1 kHz.
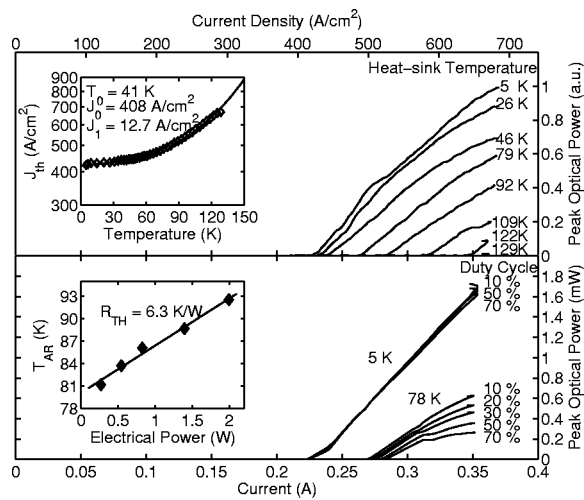
FIG. 3. Pulsed $L-I$ characteristics measured from a 40-μm-wide, 1.35-mm-long ridge laser. The upper panel shows the $L-I$s measured with 150 ns pulses repeated at 1 kHz for various heat-sink temperatures (T). The inset shows the variation of J_{th} with T along with a fit to the phenomenological relation $J_{th} = J_0 + J_1 \exp(T/T_0)$. The lower panel shows $L-I$s measured at different duty cycles when biased at 1 kHz at 5 and 78 K heat-sink temperatures. The inset plots the active region temperature T_{AR} inferred from the pulsed $J_{th}(T_{AR})$ relation versus the average electrical power dissipated in the device at threshold, as extracted from the 78 K data.

The threshold current density was $J_{th} = 419$ A/cm^2 at 5 K. A fit of J_{th} versus temperature was performed to the empirical relation $J_{th} = J_0 + J_1 \exp(T/T_0)$. Such a fit is shown in the inset of the upper panel of Fig. 3, and the characteristic temperature is extracted to be $T_0 = 41$ K, which is somewhat greater than what was obtained from our previous designs.[9] The peak current density (just before the onset of the negative differential resistance region) is nearly constant for all temperatures and is $J_{peak} \approx 700$ A/cm^2, indicating that the 55 Å injection barrier is likely the bottleneck for the current transport. Since the device lases up to a maximum temperature where $J_{th} \approx J_{peak}$, further increasing the current carrying capacity should lead to higher-temperature operation. The lower panel of Fig. 3 shows the $L-I$ characteristics for the device biased at different duty cycles at heat-sink temperatures of 5 and 78 K. Due to finite thermal resistance of the structure that arises mostly from the metal–metal bonding interface, the temperature of the active region is higher than that of the heat sink. Assuming negligible lattice heating takes place during the short pulse, the threshold current density variation plotted in the inset of the upper panel of Fig. 3 provides a measure of the active-region temperature. This J_{th} versus T relation is used to infer the active-region temperature versus the dc power dissipation (proportional to duty cycle), and we estimate a thermal resistance of $R_{th} \approx 6.3$ K/W in a lumped element approximation, as shown in the inset of the lower panel.

Information from the cw and pulsed data can be used to obtain an estimate of the thermal transport properties of the bonding interface. Figure 4 shows finite-element calculation of heat distribution in the active region and the substrate when the device is biased cw at the peak current density of $J_{peak} = 690$ A/cm^2 with the heat sink at 93 K. A thermal conductivity of $\kappa = 2$ W/cm K was assumed for the n^+ GaAs substrate,[12] and $\kappa = 0.5$ W/cm K was taken for the active re-
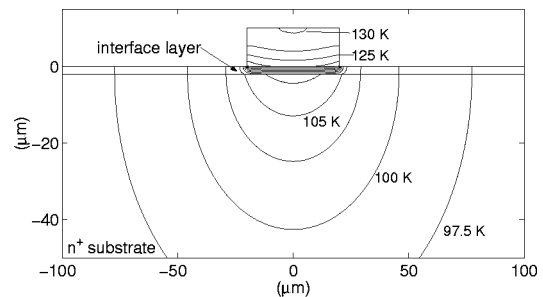

FIG. 4. Constant-temperature contour plots in the active region and the substrate with the device under dc bias at $J_{peak} = 690$ A/cm^2, and with the heat sink at 93 K, calculated using a finite element partial differential equation solver. A thermal conductivity of $\kappa = 0.1$ W/cm K is chosen as a fitting parameter for the 2-μm-thick metal–metal interface layer to yield an active-region temperature of $\sim$130 K.

gion which was experimentally measured.[13] The thermal conductivity for the 2-μm-thick alloyed In–Au interface layer was then adjusted as a fitting parameter. A value of $\kappa = 0.1$ W/cm K was necessary to yield an active region temperature of $\sim$130 K. This low value, compared to that of the semiconductor or pure indium ($\approx$1 W/cm K), indicates that the bonding interface is still the bottleneck for efficient heat removal from the device.

In conclusion, we have demonstrated a THz QCL operating cw up to 93 K, indicating the attractiveness of the resonant-phonon design and metal–metal waveguides for high-temperature operation of THz QCLs. Our investigation and analysis of thermal conduction also show that increasing the peak current densities and improving metal–metal bonding quality should lead to even higher-temperature cw operation.

[1] R. Köhler, A. Tredicucci, F. Beltram, H. E. Beere, E. H. Linfield, A. G. Davies, D. A. Ritchie, R. C. Iotti, and F. Rossi, Nature (London) **417**, 156 (2002).
[2] M. Rochat, L. Ajili, H. Willenberg, J. Faist, H. Beere, G. Davies, E. Linfield, and D. Ritchie, Appl. Phys. Lett. **81**, 1381 (2002).
[3] B. S. Williams, H. Callebaut, S. Kumar, Q. Hu, and J. L. Reno, Appl. Phys. Lett. **82**, 1015 (2003).
[4] J. Faist (private communication).
[5] G. Scalari, L. Ajili, J. Faist, H. Beere, E. Linfield, D. Ritchie, and G. Davies, Appl. Phys. Lett. **82**, 3165 (2003).
[6] R. Köhler, A. Tredicucci, F. Beltram, H. E. Beere, E. H. Linfield, A. G. Davies, D. A. Ritchie, S. S. Dhillon, and C. Sirtori, Appl. Phys. Lett. **82**, 1518 (2003).
[7] B. S. Williams, S. Kumar, H. Callebaut, Q. Hu, and J. L. Reno, Electron. Lett. **39**, 915 (2003).
[8] H. Callebaut, S. Kumar, B. S. Williams, Q. Hu, and J. L. Reno, Appl. Phys. Lett. **83**, 207 (2003).
[9] B. S. Williams, S. Kumar, H. Callebaut, Q. Hu, and J. L. Reno, Appl. Phys. Lett. **83**, 5142 (2003).
[10] B. S. Williams, S. Kumar, H. Callebaut, Q. Hu, and J. L. Reno, Appl. Phys. Lett. **83**, 2124 (2003).
[11] C. Sirtori, F. Capasso, J. Faist, A. L. Hutchinson, D. L. Sivco, and A. Y. Cho, IEEE J. Quantum Electron. **34**, 1722 (1998).
[12] J. S. Blakemore, J. Appl. Phys. **53**, R123 (1982).
[13] M. Chand and H. Maris (private communication).